

Water Resources Research

RESEARCH ARTICLE

10.1029/2018WR023889

Key Points:

- Drag forces on unsteady shallow flow over cylindrical vegetation on sloping channel are investigated after a dam break
- The resulting vegetation drag appears much smaller than predictions from uniform canopy flow experiments
- A proposed expression is experimentally tested for the dam break problem in a flume

Supporting Information:

- Supporting Information S1

Correspondence to:

M. Melis,
 s224265@studenti.polito.it

Citation:






Melis, M., Poggi, D., Fasanella, G. O. D., Cordero, S., & Katul, G. G. (2019). Resistance to flow on a sloping channel covered by dense vegetation following a dam break. *Water Resources Research*, 55. <https://doi.org/10.1029/2018WR023889>

Received 12 AUG 2018

Accepted 11 JAN 2019

Accepted article online 22 JAN 2019

Resistance to Flow on a Sloping Channel Covered by Dense Vegetation following a Dam Break

Mattia Melis^{1,2}, Davide Poggi¹, Giovanni, Oscar Domenico Fasanella¹, Silvia Cordero¹, and Gabriel G. Katul^{2,3}

¹Dipartimento di Ingegneria dell'Ambiente, del Territorio e delle Infrastrutture, Politecnico di Torino, Turin, Italy,

²Nicholas School of the Environment, Duke University, Durham, NC, USA, ³Department of Civil and Environmental Engineering, Duke University, Durham, NC, USA

Abstract The effect of hydraulic resistance on the downstream evolution of the water surface profile h in a sloping channel covered by a uniform dense rod canopy following the instantaneous collapse of a dam was examined using flume experiments. Near the head of the advancing wavefront, where h meets the rods, the conventional picture of a turbulent boundary layer was contrasted to a distributed drag force representation. The details of the boundary layer around the rod and any interferences between rods were lumped into a drag coefficient C_d . The study demonstrated the following: In the absence of a canopy, the Ritter solution agreed well with the measurements. When the canopy was represented by an equivalent wall friction as common when employing Manning's formula with constant roughness, it was possible to match the measured wavefront speed but not the precise shape of the water surface profile. However, upon adopting a distributed drag force with a constant C_d , the agreement between measured and modeled h was quite satisfactory at all positions and times. The measurements and model calculations suggested that the shape of h near the wavefront was quasilinear with longitudinal distance for a constant C_d . The computed constant C_d (≈ 0.4) was surprisingly much smaller than the C_d (≈ 1) reported in uniform flow experiments with staggered cylinders for the same element Reynolds number. This finding suggested that drag reduction mechanisms associated with unsteadiness, nonuniformity, transient waves, and other flow disturbances were more likely to play a role when compared to conventional sheltering effects.

1. Introduction

The dam break problem is associated with flow resulting from a sudden release of water behind a vertical wall or dam (Whitham, 1955). The salient features of such a flow are unsteadiness and inertia being balanced by hydrostatic pressure gradients and resistive forces. Interest in the dam break problem in hydrology and hydraulics has exponentially proliferated given their similarities to surging or flash/outburst floods in streams (Reid et al., 1998), glacial lake bursts (Carrivick, 2010), tsunami run up on coastal plains (Chanson, 2009), intense rainfall-induced overland flow over vegetated surfaces in dryland ecosystems (Assouline et al., 2015; Kefi et al., 2008; Paschalis et al., 2016; Thompson et al., 2011), peatlands (Holden et al., 2008) and tropical regions (Ajayi et al., 2008), inflow into wetlands and marshes (Kadlec, 1995; Lee et al., 2004), among others. More broadly, the mathematical form of the shallow water equations describing the flow after dam break encompasses diverse phenomenon such as thin film flows, gravity currents, and the nonlinear Fokker-Planck equation widely used in engineering, physics, chemistry, and biology (Daly & Porporato, 2004). Well-known analytical studies of the dam break problem include frictionless flows over a flat rigid surface (Ritter, 1892) and simplified wall frictional corrections to such flows (Chanson, 2009; Dressler, 1952; Hunt, 1982, 1984a, 1984b; Wang & Pan, 2015; Whitham, 1955) discussed elsewhere (Hogg & Pritchard, 2004). Moreover, extensions to steep frictionless slopes (Ancy et al., 2008) and gradual dam breaching (Capart, 2013; Ma & Fu, 2012; Wang et al., 2016) instead of instantaneous dam breaks have also been proposed.

After a dam break, the flow is generally approximated by the Saint-Venant equation (SVE) derived from the Navier-Stokes equations assuming (i) constant water density, (ii) that the water depth h is small compared with other length scales such as the wave length of the water surface or the channel width, (iii) that the pressure distribution is approximately hydrostatic so that vertical acceleration can be ignored, and (iv) that the bed slope is not too steep (de Saint-Venant, 1871). For these conditions, the continuity equation and SVE for a rectangular prismatic section of width B after a dam break are given by (French, 1985; Lighthill &

Whitham, 1955; Whitham, 1955)

$$\frac{\partial h}{\partial t} + \frac{\partial U h}{\partial x} = 0, \quad (1)$$

and

$$\frac{\partial U}{\partial t} + U \frac{\partial U}{\partial x} + g \left(\frac{\partial h}{\partial x} + S_f - S_o \right) = 0, \quad (2)$$

where x is the longitudinal distance from the dam location ($x = 0$ is at the dam location), t is time ($t = 0$ is the instant the dam is removed), h is the water depth, U is the area averaged or bulk velocity, g is the gravitational acceleration, S_o is the bed slope, and S_f is an unknown friction slope that requires further mathematical closure and frames the scope of the work here. In virtually all the aforementioned applications, the resistance law used to describe S_f is based on a locally steady and uniform flow (Bellos & Sakkas, 1987; Begnudelli & Sanders, 2007; LaRocque et al., 2012). Unsurprisingly, Manning's formula (Manning, 1891) with a constant roughness coefficient ($=n$) remains the workhorse model in use given the voluminous literature on n and its connection to the so-called Strickler scaling (Bonetti et al., 2017) or momentum roughness height (Katul et al., 2002). Such approximation yields a form of a "wall resistance law" for S_f given by

$$S_f = \left(\frac{2gn^2}{R_h^{4/3}} \right) \frac{U^2}{2g}, \quad (3)$$

where R_h is the hydraulic radius and n is in $\text{s m}^{-1/3}$ when SI units are used for all kinematic variables (adopted here). When the channel cover is densely vegetated, there is consensus that such wall resistance model may be too naive even for steady uniform flow thereby necessitating further inquiry into the explicit inclusion of distributed drag forces by vegetation elements at high Reynolds numbers (Etminan et al., 2017; Green, 2005; Huthoff et al., 2007; Huai et al., 2009; Kothiyari et al., 2009; Lawrence, 2000; Nepf, 1999, 2012; Poggi et al., 2009; Wu et al., 1999). Equation (3) assumes that energy losses occur through bed and side frictional stresses rather than a distributed drag force that can be emergent or entirely submerged (Katul et al., 2011; Marjoribanks et al., 2014; Nepf, 2012; Poggi et al., 2009). The work here explores experimentally and numerically the effects of canopy drag on S_f for such a dam break problem. The canopy used is a rigid dense cylindrical vegetation covering the flume base downstream from a dam where the slope S_o is also varied. A number of formulations have been proposed to link S_f to vegetation drag coefficient C_d assuming a steady uniform flow. These formulations, or variants on them, have been shown to capture blockage, sheltering, angle of separation, among others (Baptist et al., 2007; Carollo et al., 2002; Chapman et al., 2015; Cheng, 2015; Cheng & Nguyen, 2010; Dijkstra & Uittenbogaard, 2010; Etminan et al., 2017; James et al., 2004; Järvelä, 2002; Kouwen et al., 1969; Kim et al., 2012; Konings et al., 2012; Tanino & Nepf, 2008; Wang et al., 2015, 2018; Zhao et al., 2013). However, the dam break problem leads to transient surface waves (Kobayashi et al., 1993) as well as large horizontal gradients in Froude numbers (Ishikawa et al., 2000) not present in conventional uniform canopy flow studies. As shown here, these effects can act to reduce canopy drag well beyond standard sheltering effects.

Lastly, it is worth pointing out that despite vast life and economic losses commonly associated with dam breaks, controlled laboratory experiments on this topic remain surprisingly limited (see Table 1 in Chanson, 2009, for a review or the recent experiments in LaRocque et al., 2012). Some laboratory studies are now considering single isolated obstacles (Soares-Frazão & Zech, 2008) as may be encountered in an urban environment at high Froude numbers but not an array of obstacles. Other experiments are exclusively focused on the initial stages of the instantaneous dam break over smooth surfaces (Stansby et al., 1998) or corresponding frictional reductions via additions of polymers (Jánosi et al., 2004). Another area of growing experimental interest is contractions, expansions, and bends in the channel section after a dam failure (Frazão & Zech, 2002; Kocaman & Ozmen-Cagatay, 2012). A number of experiments have also been conducted on flow over movable beds after a dam break (Abderrezzak et al., 2008; Zech et al., 2008). However, the dam break problem for channels covered by dense vegetation that may be submerged or emergent remains understudied. Hence, the work here also fills a "data gap" by adding to the aforementioned experimental literature benchmark flume experiments where the static water level behind the dam as well as bed slope is systematically varied for a channel uniformly covered by a dense rod canopy. To further highlight the role of vegetation, the flume experiments are also repeated without any rod canopy. It is envisaged that these experiments can be

used in testing future models that include surface features explicitly in the SVE (Kesserwani & Wang, 2014) or that resolve aspects of the energetics of turbulence (Large Eddy Simulations and Direct Numerical Simulations) as discussed elsewhere (Keylock, 2015). Moreover, theories and models aimed at describing dam break wave propagation in situations where the resistance to the flow is not originating from side and bed friction (hereafter referred to as wall friction) are likely to profit from the experiments to be reported here. The majority of applications listed in section 1 fall in this aforementioned category.

2. Theory

The problem considered here is the instantaneous collapse of a dam in a long sloping prismatic rectangular channel covered by a uniform dense rod canopy chosen as a model vegetation. The cylinders comprising the rod canopy are rigid of uniform diameter D and height h_c . The goal is to describe the water level $h(x, t)$ downstream from the dam for various S_o and initial static water levels H_o behind the dam following an instantaneous dam break. To achieve this goal, the theory section is organized as follows: The case where $S_f = 0$ is first reviewed as this case sets the choice of the normalizing variables for the data analysis and model runs. Deviations between measurements and model calculations with $S_f = 0$ are used to illustrate the significance of frictional effects here. Next, various formulations linking S_f to the drag force introduced by an array of rods are provided when the flow is *locally* steady and uniform. This representation is contrasted to a Manning-type formulation that also assumes a locally steady uniform flow. The goal of this comparison is to highlight differences between wall friction and drag force representation of S_f on the shape of $h(x, t)$ within the advancing wavefront region. The determination of the most appropriate drag model and plausible choices for Manning's roughness n are discussed.

2.1. The Frictionless Case and Normalizing Variables

Since the work here considers the effects of vegetation on S_f , it is instructive to establish a reference case for an ideal flow whereby $S_f \approx 0$. When $S_f = 0$, it can be verified that the solutions to equations (1) and (2) are (Chanson, 2009; LaRocque et al., 2012)

$$U(x, t) = \frac{2}{3} \left(\frac{x}{t} + \sqrt{H_o g} + S_o g t \right) \quad (4)$$

and

$$h(x, t) = \frac{1}{9g} \left(2\sqrt{H_o g} - \frac{x}{t} + \frac{1}{2} S_o g t \right)^2, \quad (5)$$

where the initial conditions are a dry stream bed. When $S_o = 0$, equations (4) and (5) reduce to the conventional Ritter solution expressed in dimensionless form as (Ritter, 1892)

$$h_n = \frac{1}{9} (2 - u_n)^2, \quad (6)$$

where $h_n = h/H_o$ is the dimensionless water depth, $u_n = (x/t)(H_o g)^{-1/2}$ is the dimensionless wave speed, $t_n = t(H_o/g)^{-1/2}$ is dimensionless time, and $x_n = x/H_o$ is dimensionless longitudinal position downstream from the dam. Equation (6) is to be tested for the experiments reported here in the absence of vegetation.

2.2. Canopy Drag and Friction Slope

To arrive at an expression resembling equation (3) to be used in the SVE, a starting point is to also consider a locally steady uniform flow within or above a dense canopy. Moreover, the ground and side friction contribution to the total stress are ignored relative to the distributed drag force acting on the flow by the canopy elements. With these assumptions, a *local* balance between the gravitational contribution of the water weight along the longitudinal direction x and the drag force results in

$$\rho g S_f V_w = C_d A_v \rho \frac{U^2}{2g}, \quad (7)$$

where ρ is the density of water, V_w is the volume of water, A_v is the frontal area of the vegetation contained in V_w , and C_d is the drag coefficient. It is convenient to examine the force balance per unit ground area so

that $V_w = h(1 - \alpha_s \phi_v)$ and $A_v = mDh\alpha_s$, where ϕ_v is the solid volume fraction per ground area determined by $\phi_v = m\pi D^2/4$, m is the rod density determined from the number of rods per unit ground area, and α_s depends on whether the vegetation is emergent ($h/h_c > 1$) or submerged ($h/h_c < 1$). For an emergent canopy, $\alpha_s = 1$, whereas for a submerged canopy, $\alpha_s = h_c/h$ and varies with h as expected (Poggi et al., 2009). The S_f can be directly determined from equation (7) as

$$S_f = \left(\frac{C_d m D \alpha_s}{1 - \alpha_s \phi_v} \right) \frac{U^2}{2g}. \quad (8)$$

Equation (8) shows how the rod density (through m and ϕ_v) and water level (through α_s) impact S_f . The quantity that is most uncertain and encodes all the complex interactions between the canopy elements and water flow is C_d , which frames the scope here. Virtually in all studies dealing with shallow flow within vegetation, C_d is assumed to vary with a Reynolds number generically defined as $Re = VL/\nu$, where V and L are characteristic velocity and length scales, respectively, and ν is the kinematic viscosity of water. In terms of possible choices for L , the rod diameter or spacing and the hydraulic radius (or water level) have been proposed. Likewise, in terms of possible choices for V , bulk velocity, pore-scale velocity or a variant on it such as the constricted velocity, and separation velocity are commonly employed. Models for C_d that vary V (instead of L) are now reviewed.

2.2.1. The Isolated Cylinder Case

For an isolated cylinder, the local C_d (labeled as $C_{d,iso}$) can be determined from the bulk velocity and rod diameter by forming an element Reynolds number $Re_d = UD/\nu$. An approximate expression for $C_{d,iso}$ that describes data for isolated cylinders and for $Re_d < 10^5$ is given by (Cheng, 2012; Wang et al., 2015)

$$C_{d,iso} = 11(Re_d)^{-0.75} + 0.9\Gamma_1(Re_d) + 1.2\Gamma_2(Re_d), \quad (9)$$

where

$$\Gamma_1(Re_d) = 1 - \exp\left(-\frac{1000}{Re_d}\right) \quad (10)$$

and

$$\Gamma_2(Re_d) = 1 - \exp\left[-\left(\frac{Re_d}{4500}\right)^{0.7}\right]. \quad (11)$$

This expression assumes that the drag from each cylinder operates in isolation and the same U acts upon all cylinders (i.e., no interferences).

2.2.2. The Array of Cylinder Case

Several studies found that C_d in a vegetated array (hereafter referred to as $C_{d,a}$) differs from $C_{d,iso}$, and these variations do depend on the Reynolds number and ϕ_v . At a given Re_d , increasing vegetation density (or ϕ_v) appears to initially increase C_d (Stoesser et al., 2010; Tanino & Nepf, 2008) and then to decrease it (Lee et al., 2004; Nepf, 1999) for emergent canopies (Etminan et al., 2017). Such adjustment was partly accommodated by an empirical formulation for $C_{d,a}$ derived from a large synthesis of experiments on emergent vegetation and is given as (Cheng & Nguyen, 2010)

$$C_{d,a} = \frac{50}{Re_v} + 0.7 \left[1 - \exp\left(-\frac{Re_v}{15000}\right) \right]. \quad (12)$$

The linkage between the vegetation array and a stem-related Reynolds number is

$$Re_v = \frac{\pi(1 - \phi_v)}{4\phi_v} Re_d. \quad (13)$$

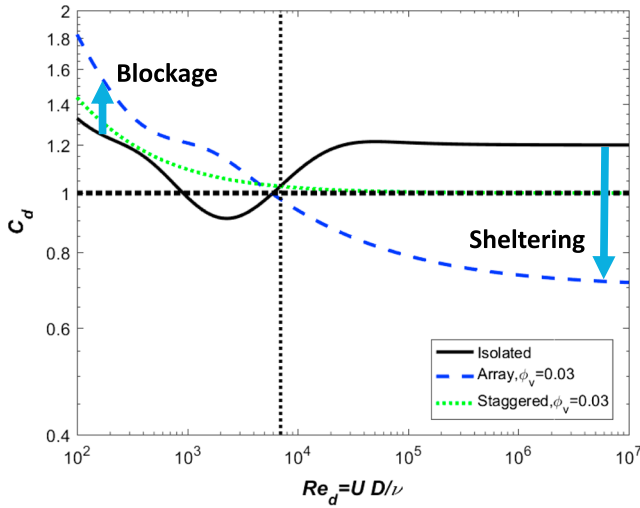


Figure 1. A comparison between C_d as a function of $Re_d = UD/v$ for an isolated cylinder (i.e., equation (9)), an array (i.e., equation (12)) of cylinders (Cheng & Nguyen, 2010) with $\phi_v = 0.03$ (the experiment here), and staggered (i.e., equation (14)) cylinders (Etminan et al., 2017) with $\lambda = (1/2)\sqrt{3}\phi_v$. At $Re_d = 0.7 \times 10^4$, the array and staggered C_d models suggest a switch from “blockage” to “sheltering” with increasing Re_d . Also, for $Re_d > \times 1 \times 10^5$, the C_d models become weakly dependent on Re_d .

2.2.4. Blockage and Sheltering Effects on C_d

Because $C_{d,iso}$ is not impacted by sheltering and blockage, it is convenient to compare the aforementioned equations for C_d (array and staggered) to assess the Re_d range where sheltering ($C_d < C_{d,iso}$) and blockage ($C_d > C_{d,iso}$) are anticipated to dominate. Sheltering indicates that some vegetation elements are located in the wake region of the upstream elements (Raupach, 1992), resulting in a lower velocity than their upstream counterparts, and generate a lower form drag compared with the isolated cylinder case. Delayed separation can be explained by the enhancement of the mean separation angle that is larger than that for the isolated cylinder, resulting in a decreasing drag coefficient compared with the isolated cylinder (Etminan et al., 2017). Both sheltering and delayed separation reduce C_d when compared to the isolated cylinder case. Blockage effects, which lead to local increases in C_d , are explained by two main factors (Etminan et al., 2017): (i) the velocity between cylinders is enhanced by the presence of vegetation and (ii) wake pressure increases drag (Zdravkovich, 2000).

The expressions for $C_{d,a}$ and $C_{d,s}$ are compared to $C_{d,iso}$ in Figure 1 for $\phi_v = 0.03$ corresponding to the flume experiments to be discussed later. This comparison is enabled by the fact that Re_v and Re_s have been related to Re_d once ϕ_v or λ are specified for a given rod density (m or S_s). Roughly, when $Re_d > 0.7 \times 10^4$, $C_{d,a}$ and $C_{d,s}$ are reduced when compared to $C_{d,iso}$ suggesting that sheltering dominates at these high Reynolds number. Conversely, when $100 < Re_d < 0.5 \times 10^4$, both $C_{d,a}$ and $C_{d,s}$ exceed $C_{d,iso}$ suggesting that blockage dominates. All three formulations also agree that for large Re_d (i.e., $Re_d > \times 10^5$), C_d becomes weakly dependent on Re_d or almost entirely independent of Re_d altogether. The operational Re_d for the flume experiments exceed 0.5×10^4 in the vicinity of the advancing wavefront.

2.3. Wall Friction Versus Distributed Drag Force: The Advancing Front Region

The water level shape of an advancing wavefront for a vegetated canopy is now contrasted to conventional Manning (or wall friction) representation of S_f with constant n using a simplified SVE. The SVE simplifications to be employed here are common to all analytical approaches describing the advancing wavefront (not the entire water surface profile though). What is novel here is the resulting link between S_f and the kinetic energy head $U^2(2g)^{-1}$. Within the wavefront region, the front speed attains a near constant value so that

Once again, this linkage allows for direct comparisons between $C_{d,iso}$ and $C_{d,a}$ at a given ϕ_v .

2.2.3. The Staggered Canopy Case

For a staggered cylindrical canopy, Etminan et al. (2017) compared C_d for various Reynolds number definitions by using differing characteristic velocity scales but maintaining $L = D$ in the definition of Re . The aforementioned work showed that typical C_d formulation for a single cylinder case can still be employed when using a constriction velocity U_c as the reference V to form $Re_s = U_c D/v$. Their resulting expression, applicable for $Re_s < 6,000$, can be summarized as

$$C_{d,s} = 1 + 10Re_s^{-2/3}, \quad (14)$$

where $Re_s = U_c D/v$ and U_c , the constriction velocity imposed by the vegetation, is related to U through the conservation of mass using

$$U_c = \frac{1}{1 - \sqrt{\frac{2\lambda}{\pi}}} U, \quad (15)$$

where $\lambda = (\pi D^2/4)/(0.5S_s^2)$ is the volume fraction for a staggered cylindrical array and S_s is the rod spacing along the flow. For uniformly spaced vegetation, $\phi_v = \lambda$ but for a staggered array, the two quantities differ because the lateral spacing of rods differ from the longitudinal spacing. Using the staggered configuration in Etminan et al. (2017), $\lambda = (1/2)\sqrt{3}\phi_v$. Equation (15) suggests that $Re_s = (1 - \sqrt{2\lambda/\pi})^{-1} Re_d$ given that both utilize $L = D$ in their definition of Re . In the limit of large $Re_s (> 5,000)$, $C_{d,s} \rightarrow 1$ and may be treated as a constant independent of Re .

$\partial U/\partial t$ and $\partial U/\partial x$ are small relative to the remaining terms in the SVE (Chanson, 2009). Also, the simplest case of a flat channel ($S_o = 0$) is considered for illustration and analytical foresight only. For these standard simplifications, the SVE reduces to its steady noninertial (diffusive wave) version given by

$$g \left(\frac{\partial h}{\partial x} + S_f \right) = 0, \quad (16)$$

and the continuity equation simplifies to

$$\frac{\partial h}{\partial t} + U \frac{\partial h}{\partial x} = 0. \quad (17)$$

At very high Re_d to be expected in the wavefront region following a dam break, C_d is likely to (i) be dominated by sheltering and (ii) becomes weakly dependent on Re_d (or almost independent) as shown in Figure 1. Hence, to a leading order in equation (8), C_d may be treated as a near constant with a numerical value that is expected to be smaller than $C_{d,iso}$ at high Re_d . Hence, the reduced SVE yields

$$U = \sqrt{-\frac{2g(1-\phi_v)}{C_d m D} \frac{\partial h}{\partial x}}, \quad (18)$$

which upon insertion into the approximated continuity equation (i.e., equation (17)) and solving the corresponding partial differential equation for h yields

$$h(x, t) = C_1 + C_2 t - \left[C_2 \sqrt{\frac{C_d m D}{2g(1-\phi_v)}} \right]^{2/3} x. \quad (19)$$

The C_1 and C_2 are integration constants to be determined from initial and boundary conditions or other constraints such as conservation of water mass or asymptotic matching to a solution near the dam location. Hence, the precise values of C_1 and C_2 vary with the specifics of the dam channel setup. However, the main (and surprising) finding here that for a near constant C_d , $h(x, t)$ is linear in x with a slope that depends on the $(C_d m D)/(1 - \phi_v)$ in the wavefront region. It is to be noted here that equation (19) assumes $h < h_c$ in the wavefront region, which is the region most impacted by the canopy drag elements. If the same analysis is repeated with equation (3) and a constant n instead of a constant C_d , the resulting U is given by

$$U = \sqrt{-\frac{h^{4/3}}{n^2} \frac{\partial h}{\partial x}}, \quad (20)$$

(i.e., nonlinear in h unless $\partial h/\partial x$ scales with $h^{-4/3}$ to ensure constant U) and the general solution of the reduced continuity equation (i.e., equation (17)) is now given by

$$h(x, t) = \left[\frac{7(t + A_1 x + A_2)}{3 A_1^3} n^2 \right]^{3/7}. \quad (21)$$

Again, A_1 and A_2 are integration constants to be determined in a manner similar to C_1 and C_2 . Upon inspecting the two general solutions in equations (21) and (19), differences between constant n (representing wall friction) and constant C_d (representing a distributed drag force acting on $h < h_c$) become apparent in the advancing wavefront region. For a constant C_d , h scales linearly with x , whereas h scales as a power law with a subunity exponent (i.e., $x^{3/7}$) for a wall friction approximation with constant n at a given time instant t . Numerical solutions to the full SVE confirm these differences and are to be discussed in comparison with the laboratory experiments proposed here.

3. Experiments

The experiments were conducted at the Giorgio Bidone hydraulics Laboratory in Politecnico di Torino, Italy. The flood wave channel, the dam and water release mechanism, the rod canopy comprising the vegetation,

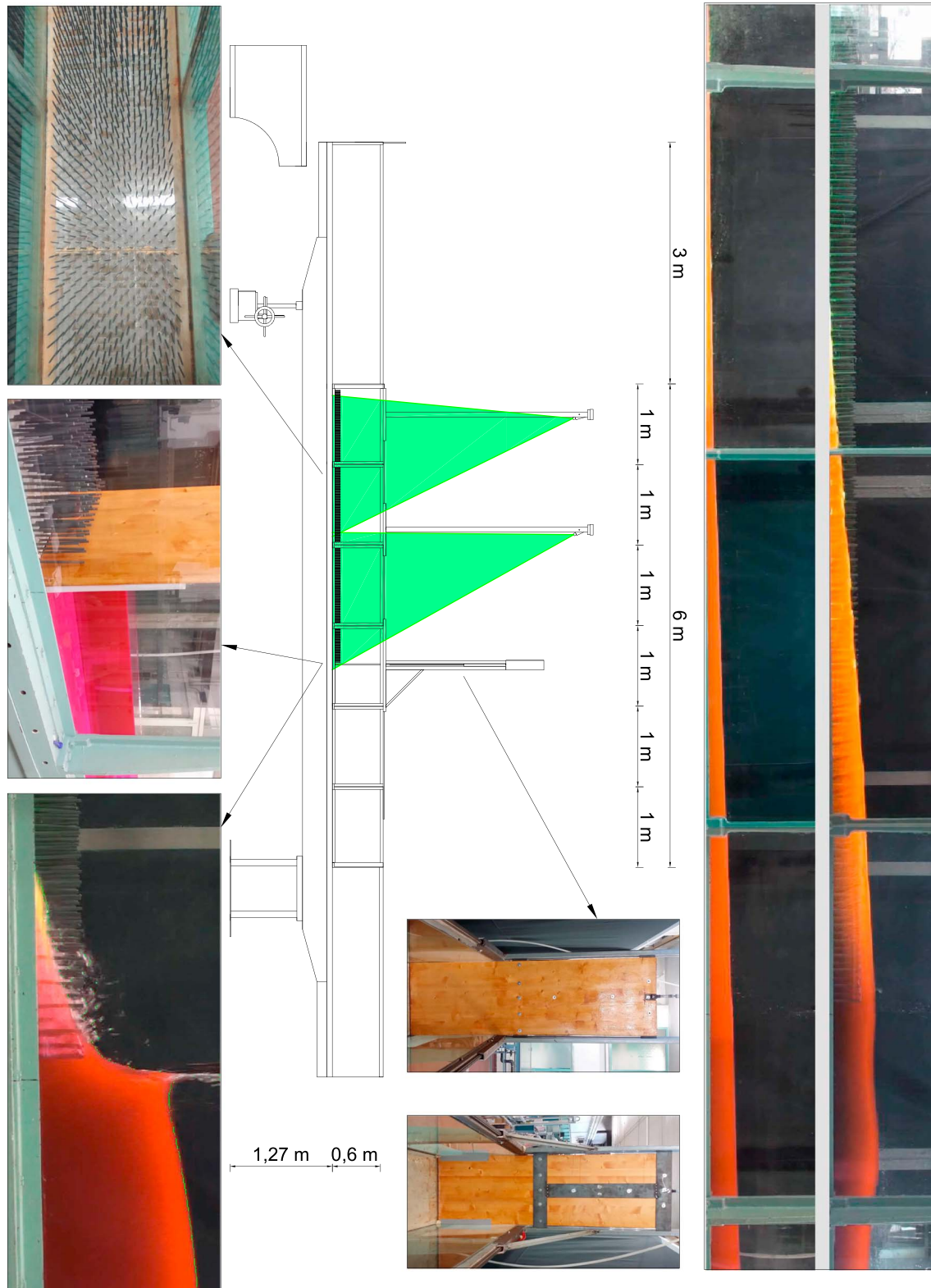


Figure 2. The experimental setup showing the channel, the dam, the dyed water behind the dam, the rod canopy representing the vegetation, and a sample image used to determine the water surface profile at one instant in time shortly after the dam break. An image showing the water level through the vegetated section is also contrasted with an image showing the water level in the absence of vegetation for $H_0 = 0.15$ m and $S_0 = 0$ (top).

the water level imaging system and data acquisition, and the test runs conducted are now described. Figure 2 shows schematically and pictorially all the aforementioned components of the experimental setup.

3.1. The Flood Wave Channel

The 11.6-m-long prismatic channel used here has a rectangular cross section that is 0.5 m ($=B$) wide and sides that are 0.6 m in height. The smooth concrete channel bottom is elevated 1.27 m from the ground floor. The channel sides are made of glass to permit optical access. The glass sides are further enforced using a steel structure. This steel structure does not allow optical access of the 0.035 m nearest to the channel bottom. A mechanical wheel allows the channel to rotate around a pin that can be adjusted so as to vary S_o from 0% to 3%. The channel is filled directly with water from below by a pipe, and the outflow from the channel discharges into a tank after passing over a rectangular weir.

3.2. The Dam Break

A wooden cofferdam with an instantaneous opening is used to model a dam break. The wood is waterproofed as this treatment allows the wood not to deteriorate during the experimental duration. The cofferdam is fixed on an aluminum double T-support and is free to move up and down through a vertical railing structure attached to the steel body of the facility. A pneumatic cylinder is fixed on top of the vertical structure and powered by a compressor located on the floor. The compressor directs an 11-bar pressure to the pneumatic cylinder forcing a disc to move rapidly upward. The disc is connected to the piston rod, which in turn is fixed to the cofferdam frame. This system uplifts the cofferdam at a speed of 0.86 m/s, thereby mimicking the instantaneous release of water into the flume following dam break.

3.3. The Vegetation

The vegetation immediately downstream from the dam is composed of an array of a polymeric resin cylinders. The cylinders are fixed onto six plastic boards each 0.15 m wide and 1.75 m long. To cover the entire cross section, the boards are positioned side by side three at a time for a total length of 3.5 m. The panels are attached to the channel bottom using silicon. This attachment allows the rods not to move during the test runs. The cylinders comprising the rod canopy are rigid with uniform diameter $D = 0.006$ m and height $h_c = 0.10$ m. The rods are arranged in a staggered configuration with a spacing of 0.035 m transversely and longitudinally, while the distance to the diagonal is 0.0175 m. This arrangement resulted in a density $m = 1,206$ rods m^{-2} . The no-vegetated case in the same facility is also tested.

3.4. Water Level Measuring Equipment and Data Acquisition

The main variable measured here is water level $h(x, t)$ variations along the channel at regular temporal intervals. To obtain $h(x, t)$ without flow interferences, three Sony Handycam HDR-XR500 cameras are used to image the water surface profile. Each camera is equipped with a 3-3/16-in. wide screen touch panel LCD, a Sony's premium G Lens and a remote control to start all cameras concurrently. This camera model is able to record high-definition AVCHD video and store it in a 120-GB hard disk. The space-time resolution used in the experiment is the best available from such a camera model ($1,920 \times 1,080$ pixels at 29.97 frames per second). The cameras are situated on a horizontal bar at a distance of 1 m from each other. They are aligned with the bottom of the channel when the slope is 0%. The distance between the cameras and the side glass is 1.5 m, thereby allowing each camera to record a movie of the full glass in its field of view. The three cameras cover a total length of 3 m starting from 0.5 m upstream of the dam. To avoid reflections from windows, two black cloths have been placed behind the cameras and behind the flood wave channel. Since water is transparent, it is difficult to automate the detection of the water surface profile from images without additional markers. For this reason, water was mixed with a Rhodamine dye that becomes fluorescent and emits red light when being excited with light at different wavelength (green light is used here). The green light is emitted by two laser generators with 200-mW power fixed over the channel on two supports welded to the metallic frame of the facility. Each laser emits a narrow beam of green light that crosses a glass cylinder with a diameter of 3 mm. When the light crosses the cylinder, it is refracted and generates a plane of light perpendicular to the bottom of the channel with the same direction as the flow. The addition of such a dye enhances the imaging and automated detection of the water surface. The calibration of the cameras is detailed in the supporting information.

3.5. Test Runs and Slope/Dam Water Level Configurations

The test runs were performed using four differing static water levels behind the dam ($H_o = 0.15, 0.20, 0.25, 0.30$ m) and four differing bed slopes ($S_o = 0\%, 1\%, 2\%, 3\%$) resulting in a total of 16 configurations. The

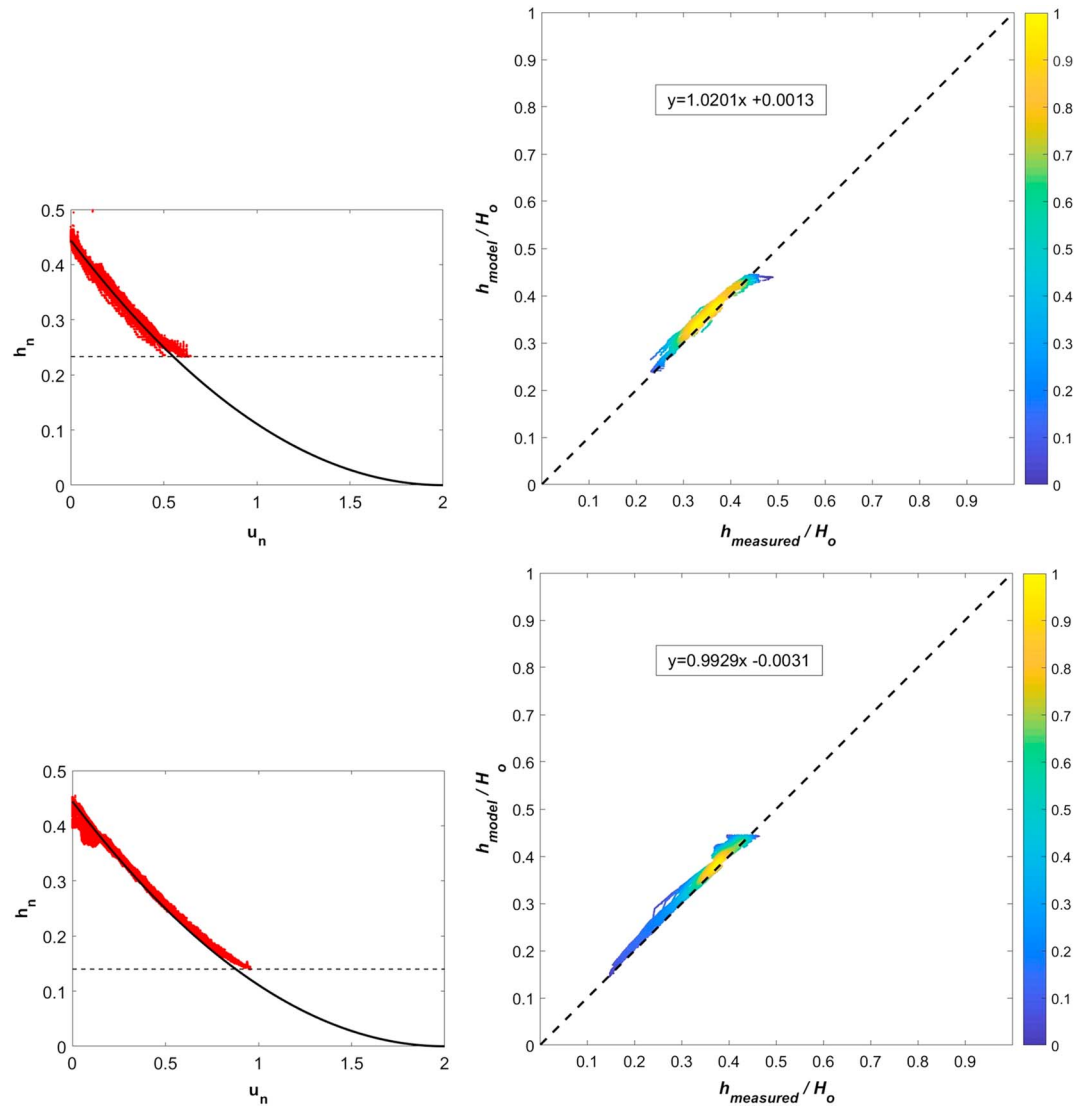


Figure 3. A comparison between measured normalized water surface $h_n = h/H_0$ (red circles) and modeled h_n (black line) using the Ritter solution for $S_0 = 0$ (left panels) and the smooth surface case. The normalized velocity is $u_n = (x/t)/\sqrt{gH_0}$. The comparisons are conducted for $H_0 = 0.15$ m (top left) and $H_0 = 0.25$ m (bottom left) and for $x > 0, t > 0$. The horizontal dashed line indicates the water level above which $h(x, t)$ is resolved with the imaging system. The one-to-one comparison between measured and modeled h_n for these two runs is also shown (right panels), where colors indicate sampling points density. The regression equations comparing measured and modeled h_n/H_0 are also shown in boxes.

0% slope configuration was repeated 10 times for each H_0 , thereby allowing the acquisition of statistically robust water level data not affected by outliers. The outcome of the analysis showed a low standard deviation between different water profiles after five replicas. This led to a decision of performing only five replicas per H_0 and S_0 configuration. Hence, water level data for each of the 16 configurations are presented as averages of the five water level replicas. For each test run, the channel slope is first configured to one of the four S_0 values. Prior to commencing a test run, the gate is closed so that a water reservoir is established behind the dam. The reservoir is filled until the desired H_0 is reached. The remaining portion downstream from the dam is initially dry. The H_0 is measured by a hydrometer fixed to the glass panel of the flume facility. The water behind the dam is then mixed with a precise amount of Rhodamine calculated in relation to the volume of water stored. The goal is to reach a color that has the same shade of red for each experiment. Once the wave channel is set, the next step is to prepare the water level imaging equipment. The two lasers are started by turning their activation key. The compressor connected to the hydraulic piston is turned on with

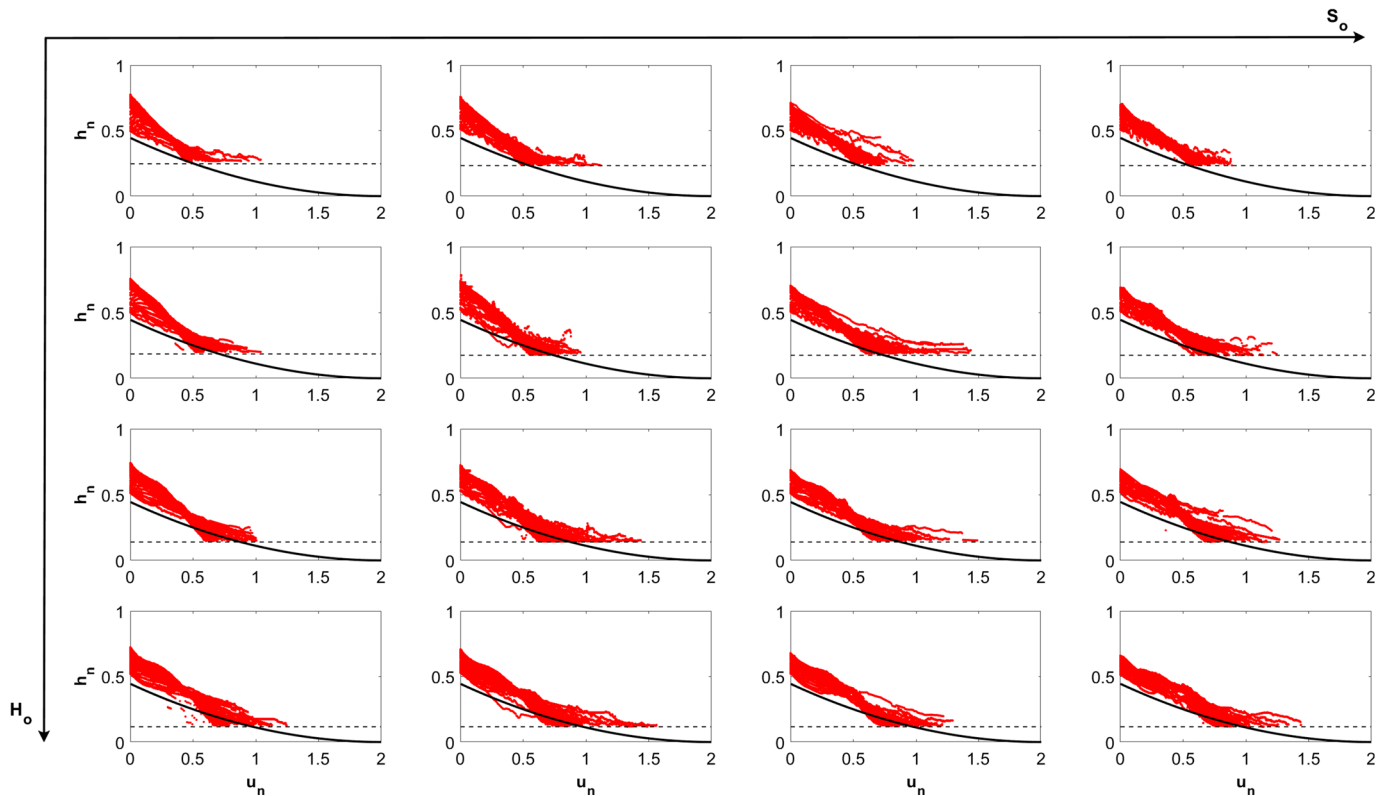


Figure 4. A comparison between measured normalized water surface $h_n = h/H_0$ (red circles) and modeled h_n (black line) using the Ritter solution for $S_0 = 0$ against normalized velocity $u_n = (x/t)/\sqrt{gH_0}$ for all 16 configurations (and $x > 0, t > 0$). Panels from left to right indicate increasing $S_0 = 0, 1, 2, 3\%$ (horizontal arrow), whereas panels from top to bottom indicate increasing $H_0 = 0.15, 0.20, 0.25, 0.30$ m (vertical arrow). The horizontal dashed line in all panels indicates the water level above which $h(x, t)$ is resolved with the imaging system.

a switch that allows it to acquire 11-bar pressure rapidly. The three cameras are turned on simultaneously with a remote controller. The test run is initiated when compressed air is pumped into the piston through a rubber pipe pulling the wooden gate of the dam up and ends when all the water is discharged. The acquired movies are converted to images and then analyzed using MATLAB (Mathworks, Natick, Massachusetts, USA). The analysis transforms the detected water level from pixel coordinates to metric coordinates thereby providing $h(x, t)$ for each run and all 16 configurations. Each run lasted from 7–10 s with the flood wave passing the entire imaged sections by the three cameras in 4–5 s. Measurements for the nonvegetated case were conducted for $H_0 = 0.15, 0.20, 0.25,$ and 0.3 m but for a flat slope. The goal of the measurements in the absence of vegetation was to explore the validity of the Ritter solution to equation (2) when $S_f = S_0 = 0$.

4. Numerical Solution of the SVE

The numerical scheme used to solve equations (1) and (2) for $h(x, t)$ and $U(x, t)$ for $x > 0$ and $t > 0$ is described elsewhere (Keskin & Ağiralioğlu, 1997). The mesh setup matches the flume experiments earlier described, where S_0 and H_0 are varied for each test run. The initial conditions are as in the flume experiments: a dry channel with $h(x, 0) = U(x, 0) = 0$ for all test runs. Two boundary conditions (i.e., $h(0, t)$ and $U(0, t)$) also require specification. The $h(0, t)$ is directly imaged and supplied from the flume experiments for each S_0 and H_0 test run. The $U(0, t)$ was not directly measured but was determined from the imaged inflow volume V_{in} into the dry channel. The $V_{in}(t)$ was then used to determine the inflow rate $Q_{in}(t) = \Delta V_{in}/\Delta t$. The inflow velocity can then be computed from the conservation of mass $U(0, t) = Q_{in}(t)/[Bh(0, t)]$. With these initial and boundary conditions, the numerical scheme was used to assess how various parametrization of S_f described by equations (3) and (8) impact $h(x, t)$. For equation (3), Manning's $n = 0.05$, which was deemed optimal for reproducing the steady state wave velocity for all 16 cases (discussed later). This value is also commensurate with many other experiments on flow through rigid emergent dense vegetation described elsewhere (Bonetti et al., 2017; Konings et al., 2012; Noarayanan et al., 2012). For equation (8), the

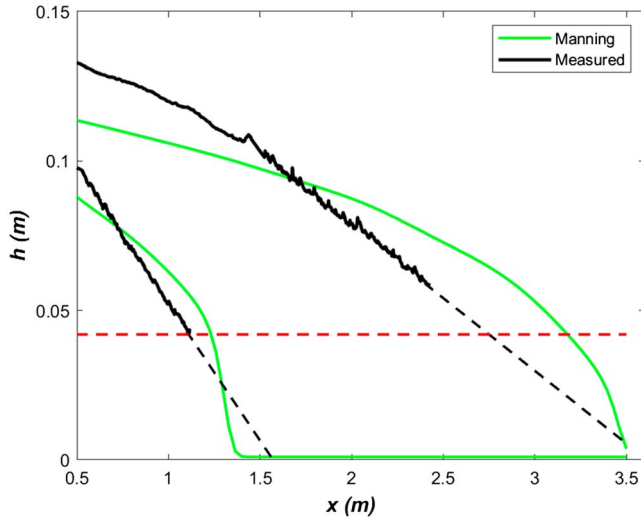


Figure 5. A comparison between measured normalized water surface $h_n = h/H_o$ (red dots) and modeled h_n (black line) using a constant $n = 0.05$. Using the linear portion of the $h(x, t)$, a near constant $C_d = 0.4$ was determined and used throughout. The horizontal dashed line indicates the water level above which $h(x, t)$ is resolved with the imaging system.

calculations were conducted using $C_{d,iso}$, $C_{d,a}$, and $C_{d,s}$ as well as a constant C_d . All these calculations were then compared to experiments imaging $h(x, t)$ for the varying H_o and S_o test runs.

5. Results

5.1. Data Summary and Comparison With the Ritter Solution

The performance of equation (6) for $H_o = 0.15, 0.20, 0.25, 0.30$ m and $S_o = 0$ was evaluated using separate experiments described elsewhere (Fasanella, 2017). The same channel and dam setup were used but without a rod canopy as shown in Figure 2. The agreement between predictions from equation (6) and the measurements for $H_o = 0.15, 0.20, 0.25, 0.3$ m was quite satisfactory for $u_n \in [0, 2]$ as shown in Figure 3. This agreement lends support to the approximations used to arrive at equation (2) in the absence of S_f when depth averaging the Navier-Stokes equations. It also suggests that the side and bed friction may be ignored relative to the other terms in the SVE for this smooth channel. These findings suggest that wall friction can be ignored relative to the canopy drag in the presence of a dense canopy.

For the vegetated canopy case, the measured $h(x, t)$ for all 16 configurations are presented in dimensionless form and compared to the Ritter solution (i.e., equation (6)) in Figure 4 shown as reference. Comparison between measurements for all x and t per test run and the Ritter solution highlights three results about the presence of a canopy: (1) the dimensionless variables selected to normalize the Ritter solution do not fully

collapse the measurements when compared to results in Figure 3, (2) the measured h/H_o is larger than predictions from the Ritter solution with the largest difference being immediately after the dam where the Ritter solution is roughly 70% of the measured values, and (3) the initial decay of h_n with increasing u_n is much steeper than predictions by equation (6) for all S_o and H_o highlighting the overall role of S_f .

5.2. Determination of C_d and n

Prior to numerically solving the SVE for all 16 test runs for the various C_d models and constant n , a preliminary estimate of C_d and n was undertaken using a small subset of water level measurements for one of the test runs ($S_o = 0$ and $H_o = 0.15$ m). An illustration is shown in Figure 5 featuring the measured water surface profile imaged at two time frames separated by about $\Delta t = 1$ s. The measurements in Figure 5 confirm the existence of a quasilinear shape for $h (< h_c)$ variations along x at the two times consistent with a constant C_d assumption employed to arrive at equation (19). Hence, equation (18) can then be used to determine C_d from measured front speed U_f (so as to avoid integration constants) as well as measured $\partial h/\partial x$, m , and ϕ_v via

$$C_d = \left(-\frac{\partial h}{\partial x} \right) \frac{2g(1-\phi_v)}{U_f^2 m D}. \quad (22)$$

At the two times shown in Figure 5, h was regressed upon x and regression slopes and intercepts recorded. The measured $\partial h/\partial x$ was then determined by averaging the two regression slopes. The front speed was determined from $U_f \approx \Delta x/\Delta t$, where Δx was determined by differencing the two computed intercepts. This distance is equivalent to extrapolating the linear water surface profiles all the way to $h = 0$ at the two times in Figure 5 and then computing the horizontal distance between these two intercepts to indicate the distance traversed by the wavefront. Using equation (22) along with $m = 1,206$ and $\phi_v = 0.03$, a $C_d = 0.4$ was computed. Because $h < h_c$ at the advancing wavefront, the low C_d here cannot be attributed to submerged vegetation effects where the bulk velocity is expected to be much higher than the velocity within canopy elements (Huthoff et al., 2007; Katul et al., 2011; Konings et al., 2012; Poggi et al., 2009). The analysis was also repeated at other times and test runs, and the outcome was similar. When averaging all outcomes, the computed $C_d \approx 0.4 \pm 0.1$. This value of C_d appears to be low (about 40% of $C_{d,s}$ reported for uniform canopy flows at high Re_d). Possible causes for such a low C_d are listed in section 6.

Equation (20) was used to compute n , thereby ensuring that U_f is matched on average, but the shape of $h(x, t)$ near the wavefront cannot be matched by wall friction models. This finding is also illustrated in

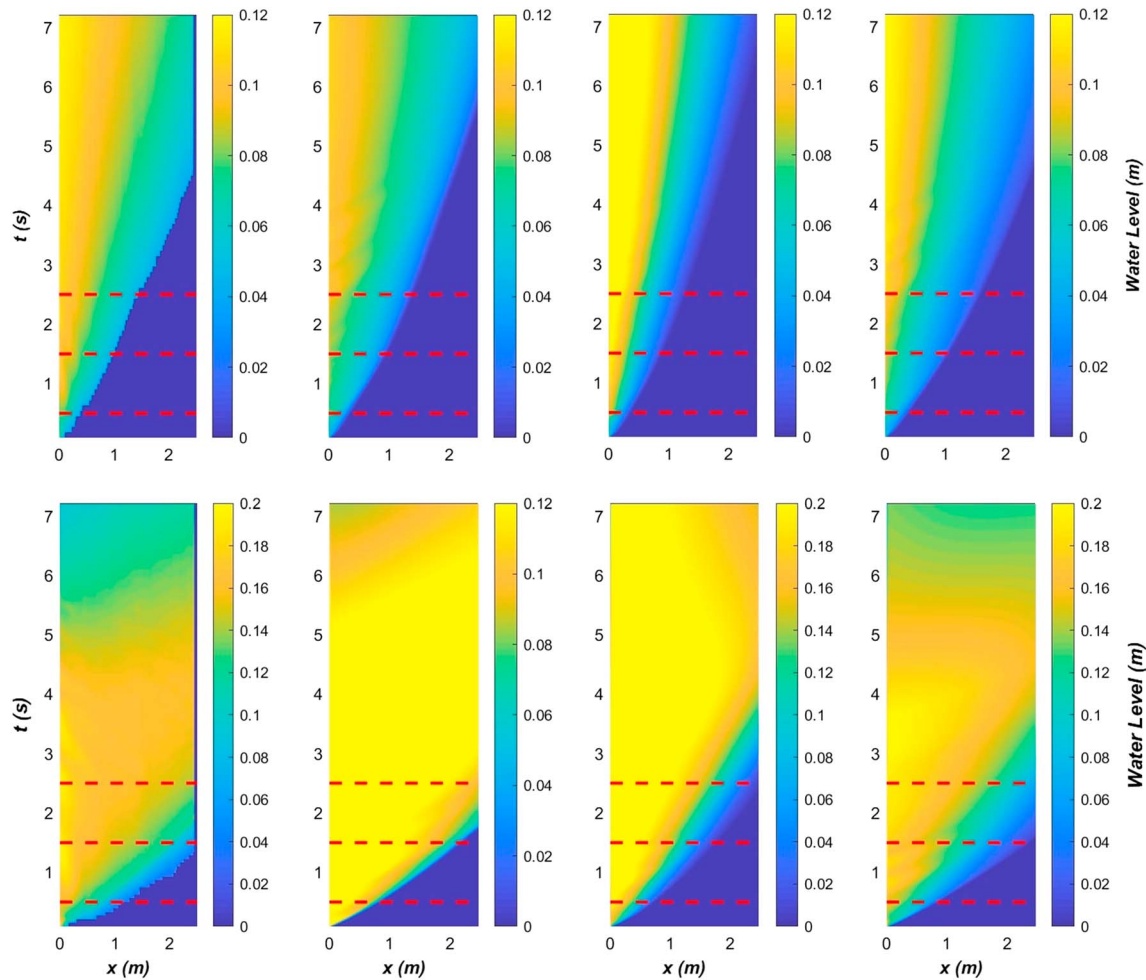


Figure 6. A comparison between measured (first column) and modeled $h(x, t)$ using Manning's S_f with a constant $n = 0.05$ (second column), the array formulation for $C_{d,a}$, and a constant $C_d = 0.4$ for the end-member test runs: $S_o = 0$ and $H_o = 0.15$ m (top row) and $S_o = 3\%$ and $H_o = 0.3$ m (bottom row). The details of the water surface profiles are compared separately for the times indicated by dashed lines.

Figure 5, where the wave speed is matched for $n = 0.05$ but not the water surface profiles as foreshadowed in section 2.3. A more expansive analysis was conducted on other test runs, and an $n = 0.05$ still appeared to reasonably reproduce the front speeds in all of them.

5.3. Comparison Between SVE and Measurements

A comparison across all runs for constant $n = 0.05$ and models of $C_{d,iso}$, $C_{d,a}$, and $C_{d,s}$ as well as $C_d = 0.4$ is conducted for all $h(x, t)$ collected in the 16 test runs. Two test run examples of such comparisons are shown in Figures 6 and 7 for Manning's formula with $n = 0.05$, $C_{d,a}$, and $C_d = 0.4$. The H_o and S_o conditions featured in the selected test runs of Figures 6 and 7 reflect the slowest and fastest wavefront (i.e., the end-members). Unsurprisingly, all models reproduce $h(x, t)$ reasonably at early times given the specified inflow hydrograph from data. However, the models begin to diverge from each other at later times as the flood wave progresses further downstream. The comparisons with measurements are suggestive that $C_d = 0.4$ (a constant) is superior to the other models. The usage of $C_{d,s}$ without any further sheltering or drag reductions overestimates $h(x, t)$ at later times (especially for the largest S_o and H_o). Similar results to $C_{d,s}$ were found for $C_{d,iso}$ and $C_{d,a}$ (results not shown). Manning's formula with $n = 0.05$ broadly captures the observed space-time patterns, but the detailed shapes of the water surface profiles are not fully recovered.

Figure 8 shows the overall comparisons between measured and modeled $h(x, t)$ using a constant $C_d = 0.4$, a constant $n = 0.05$, and the staggered drag formulation $C_{d,s}$ with no further drag reductions. Table 1 also summarizes the associated regression statistics with Figure 8 for model evaluation. The coefficient of determination (R^2) is high suggesting that all three models reproduce the space-time variability in measured water

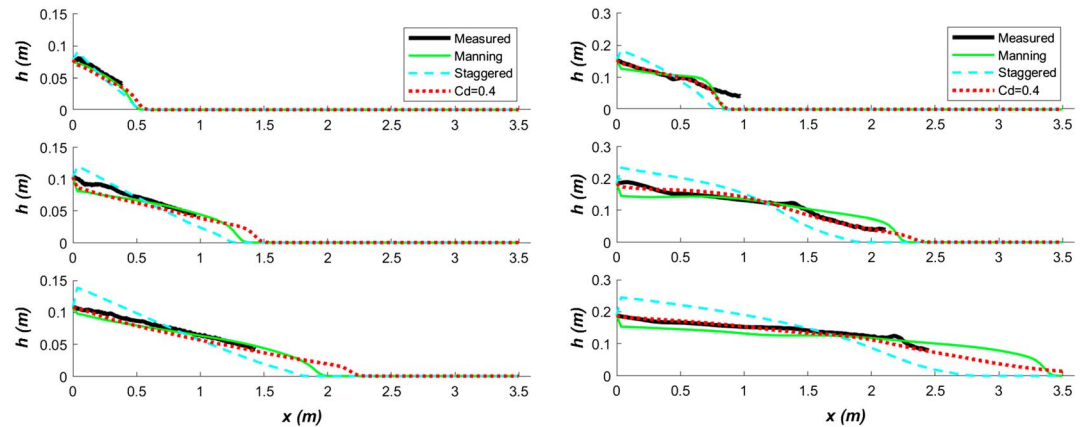


Figure 7. A comparison between measured and modeled $h(x, t)$ for the end-member test runs: $S_o = 0$ and $H_o = 0.15$ m (left column) and $S_o = 3\%$ and $H_o = 0.3$ m (right column) at times highlighted in Figure 6. Note that $h(x, t) < 0.035$ m is not resolved by the imaging system.

level. Model biases, interpreted here as regression intercept differing from zero and regression slope differing from unity, are not small for the constant n and the $C_{d,s}$ parametrization. The model calculations with $C_d = 0.4$ match closely the one-to-one line (biases are about 10%), whereas Manning's formula underestimates h in some regions and, conversely, the staggered drag coefficient formulation overestimates measured h (presumably because the resulting drag coefficient is high). When repeating the same analysis with $C_{d,iso}$ and $C_{d,a}$ (results not shown), the model data intercomparison is similar to $C_{d,s}$.

6. Discussion

For the dam break problem over vegetation, the presence of a uniform rod canopy appears to simplify the description of the water surface profile in the vicinity of the advancing wavefront because C_d becomes weakly or almost independent of the Reynolds number. This simplification is in contrast to a Manning-type representation for equivalent wall frictional effects with a constant n . An extensive linear $h(x)$ with x was predicted by this simplification for the advancing wave and was confirmed for all 16 configurations.

An unexpected result emerging from the experiments here is the significant reduction in $C_d (= 0.4)$ below its array (uniform or staggered) values reported from uniform canopy flow experiments. At high Reynolds number (but $Re_d < 3 \times 10^5$), the C_d for an isolated cylinder asymptotically approaches $C_{d,iso} = 1.2$, whereas $C_{d,s} \approx 1$ and $C_{d,a} \approx 0.8$. Reductions from $C_{d,iso}$ are commonly attributed to sheltering effects, though uniform flow experiments rarely report a factor of 3 reduction in C_d by sheltering (e.g., Figure 1). What can be the cause (or causes) of such large reductions in C_d here? With the data at hand, only speculations can be offered and their plausibility assessed. Four such speculations are now discussed.

6.1. Misalignment Between the Total Velocity Vector and the Cylinder Axis

At high Re_d , form drag dominates over viscous drag and only the velocity component perpendicular to the individual cylinder axis must be factored into the calculations of a form drag coefficient. The velocity component parallel to the cylinder axis does not contribute to the form drag. If the total velocity is U_T , then the velocity component responsible for the form drag here is $U_T \sin(\theta)$, where θ is the angle between U_T and the cylinder axis. It directly follows that deviations from $\theta = \pi/2$ must be accounted for using a drag reduction factor set to $[\sin(\theta)]^2$. To achieve a 50% reduction in C_d requires a $\theta = \pi/4$, which may not be large immediately after the dam break but is large at the tip of the advancing wavefront. If the angle formed by the imaged water surface profile and the vertical rods was used as a surrogate for θ , then θ does not drop below 0.4π (instead of $\theta = \pi/2$). Resolving θ in the vicinity of the advancing wavefront is beyond the capacity of the imaging system here. Moreover, interferences from the metallic frame of the channel make detecting the front tip using side cameras challenging. Notwithstanding this experimental limitation, the main message to be conveyed is that any misalignment between the velocity vector and the cylinder axis leads to reductions in C_d when compared to expectations from uniform flow experiments where $\theta = \pi/2$.

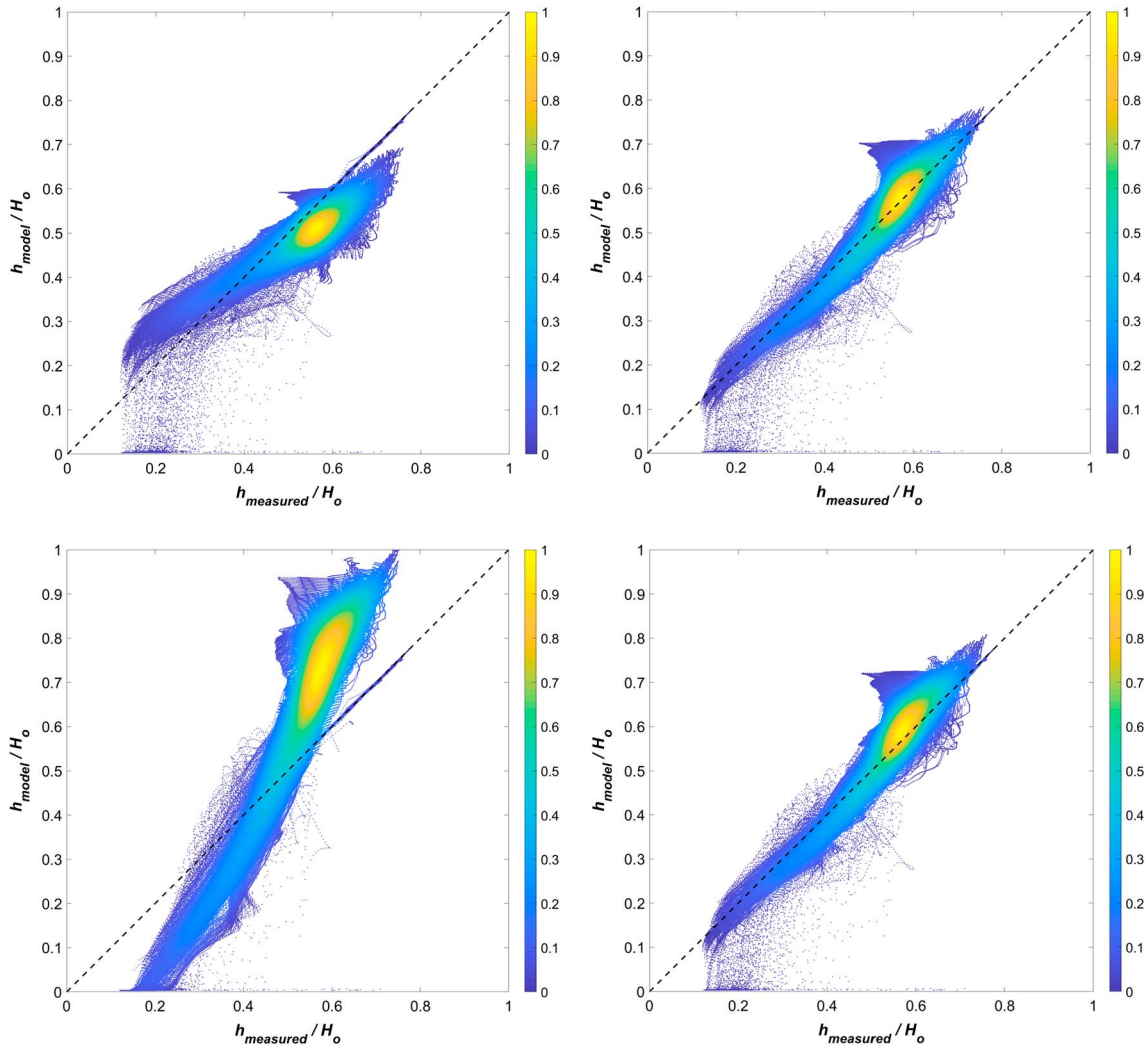


Figure 8. A comparison between measured (abscissa) and modeled (ordinate) $h(x, t)$ for all positions and times (x, t) and for all 16 runs ($> 800,000$ data points per figure) for each frictional law. The models are (top left) constant Manning's formula for wall friction ($n = 0.05$), a distributed drag force with $C_d = 0.4$ (top right), a distributed drag force with $C_d = C_{d,s}$ (bottom left), distributed drag force with $C_d = C_{d,s}$ but the asymptotic value is reduced to 0.4 instead of 1.0 (bottom right). The color maps signify density of points. The one-to-one (diagonal) line is also shown for reference.

6.2. Wave Effects

Undoubtedly, the inflow hydrograph exhibits transient waves that are likely to affect C_d . Laboratory experiments on flow within emergent dense vegetation driven by wave makers allowing for variable frequency while maintaining a mean water level constant report (Kobayashi et al., 1993)

$$C_d = 0.08 + \left(\frac{2,200}{Re_d} \right)^{2.4}. \quad (23)$$

Equation (23) is empirical but describes a range of canopy density and wave frequency. The baseline $C_d = 0.08$ value is small and is suggestive that at very high Re_d , the presence of waves act to reduce C_d versus expectations from uniform pressure or gravity-driven flows at the same Re_d . The physical mechanisms for the reduction in form drag are not too different from the one discussed in section 6.1 though inertial forces cannot be generally ignored in wave-driven flows. However, at large Keulegan-Carpenter numbers (KC), the form drag dominates over inertial forces and C_d may be interpreted as representing the total drag force acting on a cylinder. The assumption of a large KC may be plausible here when the front wave attains a quasi-constant U_f (i.e., $\partial U_f / \partial t$ is small). Transient waves do persist in the first 2–3 s out of the 7- to 10-s experiment duration here for each test run. However, these waves are not monochromatic (as in the case of a wave

Table 1

Model Evaluation Using Linear Regression (Abscissa Is Measured and Ordinate Is the Resistance Model) for the Constant Drag Coefficient $C_d = 0.4$, Constant Manning Roughness $n = 0.05$, Staggered Array Formulation $C_{d,s}$, $C_{d,s}$ -Modified, C_d -Froude, and C_d -Separation for All 16 Test Runs and All Space-Time Imaged h (> 800,000 Data Points)

Resistance Model	Slope	Intercept	R^2
$n = 0.05$	0.76	0.08	0.87
$C_d=0.4$	0.90	0.05	0.91
$C_{d,s}$	1.24	-0.03	0.87
$C_{d,s}$ -modified	0.93	0.05	0.91
C_d -Froude	0.89	0.06	0.89
C_d -Separation	0.96	0.04	0.91

Note. The coefficient of determination (R^2), the regression slope, and intercept are shown.

maker) and are superimposed on a rapid current entirely absent in wave-induced flows. For the purposes of discussion only, it may be argued that the limiting C_d at high Re_d (hereafter labeled as the asymptotic value) lies between 0.08 (for waves) and 0.8 (for uniform staggered dense canopy), with a mean value of about 0.4 as waves persisted about 50% of the inflow hydrograph period associated with the wavefront. Upstream of the rapidly advancing wavefront, the Reynolds number is lower, the water depth is gradually approaching a quasi-uniform state as evidenced by Figure 7, and $\partial C_d / \partial Re_d$ may follow expectations from uniform flow vegetation studies for staggered cylinders. These two arguments may be naively superimposed to yield

$$C_d = 0.4 + 10(Re)^{-2/3}, \quad (24)$$

which is labeled as $C_{d,s}$ -modified. A global comparison between measured and modeled $h(x, t)/H_o$ for all 16 test runs is shown in Figure 8, and the regression statistics of this comparison are summarized in Table 1. A reduction in the asymptotic value of C_d from 1.0 to 0.4 improved the comparison between measurements and model calculations over the original $C_{d,s}$, but this improvement was quite minor when referenced to $C_d = 0.4$.

6.3. Froude Number Effects

The resistance laws associated with gravity-driven flows may be viewed as expressions between a Froude number Fr and a group of dimensionless numbers, including the Reynolds number. For example, the Chezy expression where the resistance stress is expressed in kinematic form as $C_h U^2$ results in

$$Fr = \frac{U}{\sqrt{gR_h}} = \sqrt{\frac{S_o}{C_h}}, \quad (25)$$

where C_h is the Chezy constant. Rearranging this expression yields

$$C_h = \frac{S_o}{Fr^2}. \quad (26)$$

For vegetated canopies, C_h can be related to C_d , which must then be inversely related to Fr . Experimentally, it was demonstrated that (Ishikawa et al., 2000)

$$C_d = 1.24 - 0.32(Fr) \quad (27)$$

collapses measurements for emergent canopies collected for uniform flow across a wide range of ϕ_v and Re_d . For the dam break problem, the wavefront velocity U_f approaches a near constant value with increasing x ; however, $\sqrt{R_h}$ is decreasing resulting in Fr that increases with increasing x . The immediate consequence of this analysis is that $\partial Fr / \partial x$ is expected to be positive with increasing x . Based on equation (27), $\partial C_d / \partial x$ is negative in the vicinity of the wavefront due to depth nonuniformity. A C_d that only varies with $Re_d = UD/v$ simply cannot detect this decline because $U \approx U_f$ is not changing in space, whereas R_h in the vicinity of the wavefront is. The only way to accommodate this C_d decline in a C_d - Re_d expression is to artificially reduce

C_d below expectations from uniform flow in canopies (here $C_{d,s}$). Hence, it is conceivable that a reduced $C_d = 0.4$ is simply an artifact of modeling C_d by Re_d and h or R_h variations cannot be accommodated. Hence, an alternative to a $C_d - Re_d$ expression is now explored based on an expression that resembles equation (27). To maintain tractability, it was assumed that

$$C_d = a_1 + a_2(Fr)^{a_3}, \quad (28)$$

where $a_1 = 1.24$, $a_2 = -0.32$, and $a_3 = 1$ recover the best fit curve to the laboratory experiment for uniform emergent canopy flow described elsewhere (Ishikawa et al., 2000). Using the same subset of the data used to determine $n = 0.05$ and $C_d = 0.4$, best fit parameters were determined to be here $a_1 = 0.1$, $a_2 = 0.25$, and $a_3 = -0.5$. Upon comparing the values determined for the dam break problem here with those in equation (27), a number of clarifications must be made: (1) equation (27) predicts a $C_d < 0$ when $Fr > 3.87$, whereas the derived expression here predicts a saturating $C_d \approx 0.1$ for large Fr ; (2) the derived expression here predicts a $C_d \in [0.24, 0.36]$ for $Fr \in [1, 4]$ (i.e., spanning the entire super critical regime encountered in the vicinity of the modeled wavefront); (3) for $Fr < 1$, C_d increases rapidly with decreasing Fr but remains well below predictions from equation (27). It appears that the best fit C_d to equation (28) remains well below equation (27) even in the region far upstream of the wavefront where the flow is quasi-uniform. As a final check, we used $a_1 = 0.1$, $a_2 = 0.25$, and $a_3 = -0.5$ in equation (28) (labeled as C_d -Froude) to predict $h(x, t)/H_o$ for all 16 runs. A comparison between measured and modeled water levels is summarized in Table 1. Overall, the performance of the model in equation (28) is no worse than a $C_d = 0.4$ suggesting that the tendency to drop C_d below its uniform staggered arrangement value is not an artifact of the choice of an Re_d that is insensitive to R_h .

6.4. Separation and the “Drag Crisis”

For an isolated cylinder with $Re_d < 3 \times 10^5$, the boundary layer attached to the cylinder is laminar and generally separates on the front half leading to the formation of wakes behind the cylinder. For dense canopies, sheltering is linked to interactions between those wakes. The pressure in the separated region on the downstream side of an isolated cylinder is nearly constant but still smaller than the free stream pressure resulting in a large C_d . This situation was considered in prior studies dealing with separation for uniform flow within staggered vegetated systems (Etminan et al., 2017). For $Re_d > 3 \times 10^5$, the aforementioned separation mechanism becomes far more complex. The laminar boundary layer that is just beginning to form at the tip of the front half of the cylinder becomes unstable over a very short distance. The shear layer switches to a turbulent state and reattaches to the front half of the cylinder. However, this newly formed turbulent boundary layer itself separates from the cylinder on the back half. The net result is that the separation region has decreased, and the pressure in this region nearly returns to its free stream value causing a major decline in C_d that is well over 70% (for isolated cylinders). This sudden reduction in C_d is occasionally labeled as the “drag crisis” (Vogel, 1996).

While the Re_d in the wavefront region of the dam break problem is lower than 3×10^5 by an order of magnitude, the flow is highly disturbed and unsteady. In fact, the acquired movies show instances of water splashing around the rods. These large disturbances and flow unsteadiness cause rapid destabilization of the embryonic laminar boundary forming on the front side of the cylinder, thereby eliciting an early transition to turbulence. If the turbulent shear layer experiences late separation on the back side of the cylinder, then the overall bulk C_d can drop by 50%. In fact, if separation occurs midway on the back side of the cylinder, then the effective frontal area (or D_{eff}) will be reduced by a factor of 2. This reduction from D to D_{eff} alone leads to a factor of 2 reduction in $C_d m D_{\text{eff}}$ even when setting $C_d = C_{d,s}$ at the same Re_d . This scenario cannot be overlooked or dismissed and may explain the weak dependence of C_d on Re_d reported here. The necessary (but not sufficient) condition for its occurrence is that Re_d and the disturbances to the embryonic laminar boundary at the tip of the front side of the cylinders remain large to destabilize it. As an indirect check on such a separation, the calculations were repeated for the entire 16 runs with C_d set to a $C_{d,s}$ formulation using $D_{\text{eff}} = 0.5D$ (to reflect a reduction in the wake region behind the cylinder). This reduction in D also reduces Re_d , and hence, a lower Re_d and a higher C_d are expected away from the advancing wavefront with such a D_{eff} revision. The comparison between measured and modeled water levels is also summarized in Table 1. Overall, the performance of the model in equation (28) is a small improvement over the constant $C_d (= 0.4)$. That is, accentuating the Re_d effects on C_d confers minor benefits to the comparison between measured and modeled h/H_o and the separation argument may be plausible.

7. Conclusions and Broader Implications

The work here considered the effects of hydraulic resistance on the downstream evolution of the water surface profile $h(x, t)$ in a long sloping prismatic channel covered by a uniform dense rod canopy following the collapse of a dam. The focus was on the link between the sought friction slope S_f in the SVE and vegetation roughness. In particular, the way in which drag slows the propagation of the advancing wavefront was determined using three broad classes of friction models: a frictionless model with $S_f = 0$ (the Ritter solution) used as a reference, S_f described by wall or Coulomb friction (Manning's formula with constant roughness n), and a distributed drag force formulation where the drag coefficient C_d was modeled using standard equations for isolated cylinders, array of uniformly spaced cylinders, and cylinders positioned in a staggered arrangements. The following conclusions can be drawn from the experiments, model results, and simulations: (i) When setting $S_f = 0$, Ritter's solution reproduced well the measured water level in the absence of a canopy. However, it underpredicted the measured water level for a given wavefront velocity as expected in the presence of a canopy. The largest difference between measured and modeled water level was immediately after the dam but prior to the commencement of the vegetated section. At this location, the Ritter solution underpredicted the water level by some 30%. Also, with increasing wavefront speed, the measured drop in h was steeper than predictions by the Ritter solution suggesting that (gS_f) was a significant term in the SVE. (ii) When representing the canopy effects on S_f using an equivalent wall (or Coulomb) friction as common to Manning's formula with constant n , it was possible to match the measured wavefront speed with plausible values of n (≈ 0.05) but not the precise shape of h . The water surface profile from a Manning representation for S_f was shown to be a power law in x with a subunity exponent at any given t . (iii) When modeling S_f using a distributed drag force with constant C_d , agreement between measurements and model calculations was satisfactory with a coefficient of determination exceeding 0.9 and regression slopes deviating from unity by less than 10%. The model also predicted that the shape of the water surface profile near the wavefront is quasilinear in x and can be theoretically linked to C_d . (iv) A computed constant $C_d \approx 0.4$ from such links is much smaller than C_d reported for uniform flow experiments with staggered cylinders at the same element Reynolds number. This suggests that drag reduction mechanisms associated with nonuniformity, unsteadiness and transient waves, and flow disturbances are more likely when compared to conventional sheltering effects.

The broader implications of this work highlights a need for new frictional laws describing S_f in disturbed nonsteady nonuniform flow conditions beyond conventional wall or Coulomb friction representations. These developments are likely to be imminently used when combining such models for closing the SVE with water level data acquired from space (Alsdorf et al., 2001, 2000, 2007). There is some urgency for progress on this front as climate change may result in more frequent flooding events, and improving flood warning and monitoring systems is of obvious societal significance.

Acknowledgments

M. Melis acknowledges Politecnico di Torino (Italy) for supporting the visit to Duke University. G. Katul acknowledges support from the U.S. National Science Foundation (NSF-EAR-1344703, NSF-AGS-1644382, and NSF-IOS-1754893). D. Poggi acknowledges support from EU Territorial co-operation Program INTERREG (Alcotra), project RESBA-1729. The data are publicly available and can be downloaded from the Duke University Library Digital Repository at <https://doi.org/10.7924/r4t72c41h>.

References

- Abderrezzak, K. E. K., Paquier, A., & Gay, B. (2008). One-dimensional numerical modelling of dam-break waves over movable beds: Application to experimental and field cases. *Environmental Fluid Mechanics*, 8(2), 169–198.
- Ajayi, A. E., van de Giesen, N., & Vlek, P. (2008). A numerical model for simulating Hortonian overland flow on tropical hillslopes with vegetation elements. *Hydrological Processes*, 22(8), 1107–1118. <https://doi.org/10.1002/hyp.6665>
- Alsdorf, D., Birkett, C., Dunne, T., Melack, J., & Hess, L. (2001). Water level changes in a large Amazon lake measured with spaceborne radar interferometry and altimetry. *Geophysical Research Letters*, 28(14), 2671–2674.
- Alsdorf, D. E., Melack, J. M., Dunne, T., Mertes, L. A., Hess, L. L., & Smith, L. C. (2000). Interferometric radar measurements of water level changes on the Amazon flood plain. *Nature*, 404(6774), 174.
- Alsdorf, D. E., Rodríguez, E., & Lettenmaier, D. P. (2007). Measuring surface water from space. *Reviews of Geophysics*, 45, RG2002. <https://doi.org/10.1029/2006RG000197>
- Ancey, C., Iverson, R., Rentschler, M., & Denlinger, R. (2008). An exact solution for ideal dam-break floods on steep slopes. *Water Resources Research*, 44, W01430. <https://doi.org/10.1029/2007WR006353>
- Assouline, S., Thompson, S., Chen, L., Svoray, T., Sela, S., & Katul, G. (2015). The dual role of soil crusts in desertification. *Journal of Geophysical Research: Biogeosciences*, 120, 2108–2119. <https://doi.org/10.1002/2015JG003185>
- Baptist, M., Babovic, V., Rodríguez Uthurburu, J., Keijzer, M., Uittenbogaard, R., Mynett, A., & Verwey, A. (2007). On inducing equations for vegetation resistance. *Journal of Hydraulic Research*, 45(4), 435–450.
- Begnudelli, L., & Sanders, B. F. (2007). Simulation of the St. Francis dam-break flood. *Journal of Engineering Mechanics*, 133(11), 1200–1212.
- Bellos, C. V., & Sakkas, J. G. (1987). 1-D dam-break flood-wave propagation on dry bed. *Journal of Hydraulic Engineering*, 113(12), 1510–1524.
- Bonetti, S., Manoli, G., Manes, C., Porporato, A., & Katul, G. G. (2017). Manning's formula and Strickler's scaling explained by a co-spectral budget model. *Journal of Fluid Mechanics*, 812, 1189–1212.

- Capart, H. (2013). Analytical solutions for gradual dam breaching and downstream river flooding. *Water Resources Research*, *49*, 1968–1987. <https://doi.org/10.1002/wrcr.20167>
- Carollo, F. G., Ferro, V., & Termini, D. (2002). Flow velocity measurements in vegetated channels. *Journal of Hydraulic Engineering*, *128*(7), 664–673.
- Carrivick, J. L. (2010). Dam break–outburst flood propagation and transient hydraulics: A geosciences perspective. *Journal of Hydrology*, *380*(3–4), 338–355.
- Chanson, H. (2009). Application of the method of characteristics to the dam break wave problem. *Journal of Hydraulic Research*, *47*(1), 41–49.
- Chapman, J. A., Wilson, B. N., & Gulliver, J. S. (2015). Drag force parameters of rigid and flexible vegetal elements. *Water Resources Research*, *51*, 3292–3302. <https://doi.org/10.1002/2014WR015436>
- Cheng, N.-S. (2012). Calculation of drag coefficient for arrays of emergent circular cylinders with pseudofluid model. *Journal of Hydraulic Engineering*, *139*(6), 602–611.
- Cheng, N.-S. (2015). Single-layer model for average flow velocity with submerged rigid cylinders. *Journal of Hydraulic Engineering*, *141*(10), 06015012.
- Cheng, N.-S., & Nguyen, H. T. (2010). Hydraulic radius for evaluating resistance induced by simulated emergent vegetation in open-channel flows. *Journal of Hydraulic Engineering*, *137*(9), 995–1004.
- Daly, E., & Porporato, A. (2004). Similarity solutions of nonlinear diffusion problems related to mathematical hydraulics and the Fokker-Planck equation. *Physical Review E*, *70*(5), 056303.
- de Saint-Venant, A. B. (1871). Theorie du mouvement non permanent des eaux, avec application aux crues des rivieres et a l'introduction des marees dans leurs lits. *Comptes Rendus des seances de l'Academie des Sciences*, *73*, 237–240.
- Dijkstra, J., & Uittenbogaard, R. (2010). Modeling the interaction between flow and highly flexible aquatic vegetation. *Water Resources Research*, *46*, W12547. <https://doi.org/10.1029/2010WR009246>
- Dressler, R. F. (1952). *Hydraulic resistance effect upon the dam-break functions*. Washington, DC: National Bureau of Standards.
- Etminan, V., Lowe, R. J., & Ghisalberti, M. (2017). A new model for predicting the drag exerted by vegetation canopies. *Water Resources Research*, *53*, 3179–3196. <https://doi.org/10.1002/2016WR020090>
- Fasanella, G. (2017). Studio sperimentale dell'influenza di macroscabrezze sulla propagazione di onde di piena. Tesi di Laurea Magistrale.
- Frazão, S. S., & Zech, Y. (2002). Dam break in channels with 90° bend. *Journal of Hydraulic Engineering*, *128*(11), 956–968.
- French, R. H. (1985). *Open-channel hydraulics*. New York: McGraw-Hill.
- Green, J. C. (2005). Modelling flow resistance in vegetated streams: Review and development of new theory. *Hydrological Processes*, *19*(6), 1245–1259.
- Hogg, A. J., & Pritchard, D. (2004). The effects of hydraulic resistance on dam-break and other shallow inertial flows. *Journal of Fluid Mechanics*, *501*, 179–212.
- Holden, J., Kirkby, M. J., Lane, S. N., Milledge, D. G., Brookes, C. J., Holden, V., & McDonald, A. T. (2008). Overland flow velocity and roughness properties in peatlands. *Water Resources Research*, *44*, W06415. <https://doi.org/10.1029/2007WR006052>
- Huai, W.-X., Zeng, Y.-H., Xu, Z.-G., & Yang, Z.-H. (2009). Three-layer model for vertical velocity distribution in open channel flow with submerged rigid vegetation. *Advances in Water Resources*, *32*(4), 487–492.
- Hunt, B. (1982). Asymptotic solution for dam-break problem. *Journal of the Hydraulics Division*, *108*(1), 115–126.
- Hunt, B. (1984a). Dam-break solution. *Journal of Hydraulic Engineering*, *110*(6), 675–686.
- Hunt, B. (1984b). Perturbation solution for dam-break floods. *Journal of Hydraulic Engineering*, *110*(8), 1058–1071.
- Huthoff, F., Augustijn, D., & Hulscher, S. J. (2007). Analytical solution of the depth-averaged flow velocity in case of submerged rigid cylindrical vegetation. *Water Resources Research*, *43*, W06413. <https://doi.org/10.1029/2006WR005625>
- Ishikawa, Y., Mizuhara, K., & Ashida, S. (2000). Effect of density of trees on drag exerted on trees in river channels. *Journal of Forest Research*, *5*(4), 271–279.
- James, C., Birkhead, A., Jordanova, A., & O'sullivan, J. (2004). Flow resistance of emergent vegetation. *Journal of Hydraulic Research*, *42*(4), 390–398.
- Jánosi, I. M., Jan, D., Szabó, K. G., & Tél, T. (2004). Turbulent drag reduction in dam-break flows. *Experiments in Fluids*, *37*(2), 219–229.
- Järvelä, J. (2002). Flow resistance of flexible and stiff vegetation: A flume study with natural plants. *Journal of Hydrology*, *269*(1), 44–54.
- Kadlec, R. H. (1995). Overview: Surface flow constructed wetlands. *Water Science and Technology*, *32*(3), 1–12.
- Katul, G. G., Poggi, D., & Ridolfi, L. (2011). A flow resistance model for assessing the impact of vegetation on flood routing mechanics. *Water Resources Research*, *47*, W08533. <https://doi.org/10.1029/2010WR010278>
- Katul, G. G., Wiberg, P., Albertson, J., & Hornberger, G. (2002). A mixing layer theory for flow resistance in shallow streams. *Water Resources Research*, *38*(11), 1250. <https://doi.org/10.1029/2001WR000817>
- Kefi, S., Rietkerk, M., & Katul, G. G. (2008). Vegetation pattern shift as a result of rising atmospheric CO₂ in arid ecosystems. *Theoretical Population Biology*, *74*(4), 332–344.
- Keskin, M. E., & Ağiralioğlu, N. (1997). A simplified dynamic model for flood routing in rectangular channels. *Journal of Hydrology*, *202*(1–4), 302–314.
- Kesserwani, G., & Wang, Y. (2014). Discontinuous Galerkin flood model formulation: Luxury or necessity? *Water Resources Research*, *50*, 6522–6541. <https://doi.org/10.1002/2013WR014906>
- Keylock, C. J. (2015). Flow resistance in natural, turbulent channel flows: The need for a fluvial fluid mechanics. *Water Resources Research*, *51*, 4374–4390. <https://doi.org/10.1002/2015WR016989>
- Kim, J., Ivanov, V. Y., & Katopodes, N. D. (2012). Hydraulic resistance to overland flow on surfaces with partially submerged vegetation. *Water Resources Research*, *48*, W10540. <https://doi.org/10.1029/2012WR012047>
- Kobayashi, N., Raichle, A. W., & Asano, T. (1993). Wave attenuation by vegetation. *Journal of Waterway, Port, Coastal, and Ocean Engineering*, *119*(1), 30–48.
- Kocaman, S., & Ozmen-Cagatay, H. (2012). The effect of lateral channel contraction on dam break flows: Laboratory experiment. *Journal of Hydrology*, *432*, 145–153.
- Konings, A. G., Katul, G. G., & Thompson, S. E. (2012). A phenomenological model for the flow resistance over submerged vegetation. *Water Resources Research*, *48*, W02522. <https://doi.org/10.1029/2011WR011000>
- Kothiyari, U. C., Hayashi, K., & Hashimoto, H. (2009). Drag coefficient of unsubmerged rigid vegetation stems in open channel flows. *Journal of Hydraulic Research*, *47*(6), 691–699.
- Kouwen, N., Unny, T., & Hill, H. M. (1969). Flow retardance in vegetated channels. *Journal of the Irrigation and Drainage Division*, *95*(2), 329–344.

- LaRocque, L. A., Imran, J., & Chaudhry, M. H. (2012). Experimental and numerical investigations of two-dimensional dam-break flows. *Journal of Hydraulic Engineering*, *139*(6), 569–579.
- Lawrence, D. (2000). Hydraulic resistance in overland flow during partial and marginal surface inundation: Experimental observations and modeling. *Water Resources Research*, *36*(8), 2381–2393.
- Lee, J. K., Roig, L. C., Jenter, H. L., & Visser, H. M. (2004). Drag coefficients for modeling flow through emergent vegetation in the Florida Everglades. *Ecological Engineering*, *22*(4–5), 237–248.
- Lighthill, M., & Whitham, G. (1955). On kinematic waves. I. Flood movement in long rivers. *Proceedings of the Royal Society of London. Series A, Mathematical and Physical Sciences*, *229*, 281–316.
- Ma, H., & Fu, X. (2012). Real time prediction approach for floods caused by failure of natural dams due to overtopping. *Advances in Water Resources*, *35*, 10–19.
- Manning, R. (1891). On the flow of water in open channels and pipes. *Transactions of the Institution of Civil Engineers of Ireland*, *20*(5–6), 161–207.
- Marjoribanks, T. I., Hardy, R. J., & Lane, S. N. (2014). The hydraulic description of vegetated river channels: The weaknesses of existing formulations and emerging alternatives. *Wiley Interdisciplinary Reviews: Water*, *1*(6), 549–560.
- Nepf, H. (1999). Drag, turbulence, and diffusion in flow through emergent vegetation. *Water Resources Research*, *35*(2), 479–489.
- Nepf, H. M. (2012). Flow and transport in regions with aquatic vegetation. *Annual Review of Fluid Mechanics*, *44*, 123–142.
- Noorayanan, L., Murali, K., & Sundar, V. (2012). Manning's coefficient for flexible emergent vegetation in tandem configuration. *Journal of Hydro-environment Research*, *6*(1), 51–62.
- Paschalis, A., Katul, G. G., Faticchi, S., Manoli, G., & Molnar, P. (2016). Matching ecohydrological processes and scales of banded vegetation patterns in semi-arid catchments. *Water Resources Research*, *52*, 2259–2278. <https://doi.org/10.1002/2015WR017679>
- Poggi, D., Krug, C., & Katul, G. G. (2009). Hydraulic resistance of submerged rigid vegetation derived from first-order closure models. *Water Resources Research*, *45*, W10442. <https://doi.org/10.1029/2008WR007373>
- Raupach, M. (1992). Drag and drag partition on rough surfaces. *Boundary-Layer Meteorology*, *60*(4), 375–395.
- Reid, I., Laronne, J. B., & Powell, D. M. (1998). Flash-flood and bedload dynamics of desert gravel-bed streams. *Hydrological Processes*, *12*(4), 543–557.
- Ritter, A. (1892). Die fortpflanzung der wasserwellen. *Zeitschrift des Vereines Deutscher Ingenieure*, *36*(33), 947–954.
- Soares-Frazão, S., & Zech, Y. (2008). Dam-break flow through an idealised city. *Journal of Hydraulic Research*, *46*(5), 648–658.
- Stansby, P., Chegini, A., & Barnes, T. (1998). The initial stages of dam-break flow. *Journal of Fluid Mechanics*, *374*, 407–424.
- Stoesser, T., Kim, S., & Diplas, P. (2010). Turbulent flow through idealized emergent vegetation. *Journal of Hydraulic Engineering*, *136*(12), 1003–1017.
- Tanino, Y., & Nepf, H. M. (2008). Laboratory investigation of mean drag in a random array of rigid, emergent cylinders. *Journal of Hydraulic Engineering*, *134*(1), 34–41.
- Thompson, S., Katul, G., Konings, A., & Ridolfi, L. (2011). Unsteady overland flow on flat surfaces induced by spatial permeability contrasts. *Advances in Water Resources*, *34*(8), 1049–1058.
- Vogel, S. (1996). *Life in moving fluids: The physical biology of flow*. Princeton, NJ: Princeton University Press.
- Wang, B., Chen, Y., Wu, C., Dong, J., Ma, X., & Song, J. (2016). A semi-analytical approach for predicting peak discharge of floods caused by embankment dam failures. *Hydrological Processes*, *30*(20), 3682–3691.
- Wang, W.-J., Huai, W.-X., Thompson, S., & Katul, G. G. (2015). Steady nonuniform shallow flow within emergent vegetation. *Water Resources Research*, *51*, 10,047–10,064. <https://doi.org/10.1002/2015WR017658>
- Wang, W.-J., Huai, W.-X., Thompson, S., Peng, W.-Q., & Katul, G. G. (2018). Drag coefficient estimation using flume experiments in shallow non-uniform water flow within emergent vegetation during rainfall. *Ecological Indicators*, *92*, 367–378.
- Wang, L.-H., & Pan, C.-H. (2015). An analysis of dam-break flow on slope. *Journal of Hydrodynamics, Series B*, *26*(6), 902–911.
- Whitham, G. B. (1955). The effects of hydraulic resistance in the dam-break problem. *Proceedings of the Royal Society of London: A*, *227*(1170), 399–407.
- Wu, F. C., Shen, H. W., & Chou, Y. J. (1999). Variation of roughness coefficients for unsubmerged and submerged vegetation. *Journal of Hydraulic Engineering*, *125*(9), 934–942.
- Zdravkovich, M. M. (2000). *Flow around circular cylinders: Applications*. United Kingdom: Oxford University Press, Oxford.
- Zech, Y., Soares-Frazão, S., Spinewine, B., & Le Grelle, N. (2008). Dam-break induced sediment movement: Experimental approaches and numerical modelling. *Journal of Hydraulic Research*, *46*(2), 176–190.
- Zhao, K., Cheng, N. S., Wang, X., & Tan, S. K. (2013). Measurements of fluctuation in drag acting on rigid cylinder array in open channel flow. *Journal of Hydraulic Engineering*, *140*(1), 48–55.